Large anomalous Hall, Nernst effect and topological phases in the 3d-4d/5d based oxide double perovskites

Kartik Samanta

Jonathan Noky

Iñigo Robredo

Juergen Kuebler

Maia G. Vergniory

See next page for additional authors

Authors

Kartik Samanta, Jonathan Noky, Iñigo Robredo, Juergen Kuebler, Maia G. Vergniory, and Claudia Felser

ARTICLE   OPEN

Check for updates

Large anomalous Hall, Nernst effect and topological phases in the 3d-4d/5d-based oxide double perovskites

Kartik Samanta[1,4✉], Jonathan Noky[1], Iñigo Robredo[1,2], Juergen Kuebler[3], Maia G. Vergniory[1,2✉] and Claudia Felser [1✉]

Magnetism and spin-orbit coupling are two fundamental and interconnected properties of oxide materials, that can give rise to various topological transport phenomena, including anomalous Hall and anomalous Nernst effects. These transport responses can be significantly enhanced by designing an electronic structure with a large Berry curvature. In this context, rocksalt-ordered double perovskites (DP), denoted as $A_2BB'O_6$, with two distinct transition metal sites are very powerful platforms for exploration and research. In this work, we present a comprehensive study based on the intrinsic anomalous transport in cubic and tetragonal stable DP compounds with 3d-4d/5d elements. Our findings reveal that certain DP compounds show a large anomalous Hall effect, displaying topological band crossings in the proximity of the Fermi energy.

INTRODUCTION

Since the theoretical prediction of topological insulators[1–4] and topological semi-metals[5–7], researchers in the field of condensed matter and materials science have extensively endeavored to design, characterize, and synthesize topological materials[3,4,6,8] considering their potential applicability in the field of quantum information[9], coherent spin transport[10], and high-efficiency catalysis[11]. Recent advances in elementary band representation theory have accelerated the prediction of insulating and (semi-) metallic non-magnetic and magnetic topological phases of matter in real materials[12–18]. However, the prediction of stable magnetic topological materials with large transport characteristics such as large anomalous Hall conductivity (AHC) and Nernst conductivity (ANC) in strongly correlated magnetic oxides is more challenging, and systematic calculations have been conducted only for a few selected strongly correlated oxides[19–28].

In correlated magnetic systems, the interplay between magnetism, crystal symmetry, and spin-orbit coupling (SOC) underlies the various topological transport phenomena and is highly intriguing from an experimental perspective[29–31]. In three-dimensional (3D) ferromagnets, spin-polarized bands often display topologically non-trivial nodal points and nodal lines (NLs)[32–38]. The lifting of band degeneracy because of the SOC around a nodal structure gives rise to increased Berry curvature around it, leading to a variety of topological transport phenomena, including the anomalous Hall effect (AHE) as well as the anomalous Nernst effect (ANE)[35,39–41].

In the case of magnetic topological materials with large AHC and ANC conductivities, it is important to have a magnetic site with a localized magnetic moment, which can provide a high energy scale for magnetism, as well as a magnetic site occupied by a heavy element with strong SOC. From the perspective of designing magnetic topological materials, it is also important to have materials with physically separated ions that host magnetism and ions that host strong SOC, to avoid the problem resulting from the interplay between the correlation effect and SOC at the same site. A promising class of materials in this context is the rocksalt-ordered[42] double perovskite (DP) compounds with the general formula $A_2BB'O_6$. These compounds present the possibility of hosting a 3d transition metal (TM) ion at the B site and 4d/5d TM ions at the B' site, offering a suitable playground for exploring exotic properties that depend on the competing energy scales associated with the bandwidth, Coulomb correlation, and SOC for the 3d and 4d/5d orbitals at these two sites. From an experimental point of view, these compounds are easy to produce, are robustly stable against oxidation in ambient air, and possess a high magnetic ordering temperature. However, because most conventional topological materials have low transition temperatures, their application to potential technologies is complicated. Several prominent 3d-4d/5d DP compounds with remarkable properties, such as half-metallicity at room temperature[43] and colossal magnetoresistance[44] are known. These compounds are excellent candidates for real-life applications, such as spintronics and low-dissipation devices[45]. In addition, in many of these 3d-4d/5d DP materials, the low-energy physics is primarily governed by the t_{2g}-orbital bands of the 4d/5d TM ions with strong SOC, with the possibility of a topological band crossing near the Fermi energy with highly efficient transport characteristics, such as AHC and ANC. In spite of the extensive studies of the electronic and magnetic properties of these materials[46–49], the topological characteristics of these materials have not yet been adequately investigated. This motivated our study, in which we considered selected cubic and tetragonal 3d-4d/5d-based experimentally reported DP with the aim to explore and understand stable topological materials with large AHC and ANC. Our results show the possible existence of a clean topological band crossing near the Fermi energy, primarily contributed by the $5d$-t_{2g} orbitals with large AHC and ANC. In certain DP compounds, particularly in Ba_2NiReO_6, a mirror symmetry-protected topological nodal line and their drumhead surface state are observed very close to the Fermi energy. In addition, the AHC and ANC of these compounds are almost three times larger than those of the extensively studied prototype metallic ferromagnetic oxide material $SrRuO_3$[19,41].

[1]Max Planck Institute for Chemical Physics of Solids, 01187 Dresden, Germany. [2]Donostia International Physics Center, 20018 Donostia - San Sebastián, Spain. [3]Technische Universitaet Darmstadt, 64289 Darmstadt, Germany. [4]Present address: Department of Physics and Astronomy, University of Nebraska-Lincoln, Lincoln, NE 68588, USA. ✉email: Kartik.Samanta@cpfs.mpg.de; Maia.Vergniory@cpfs.mpg.de; Claudia.Felser@cpfs.mpg.de
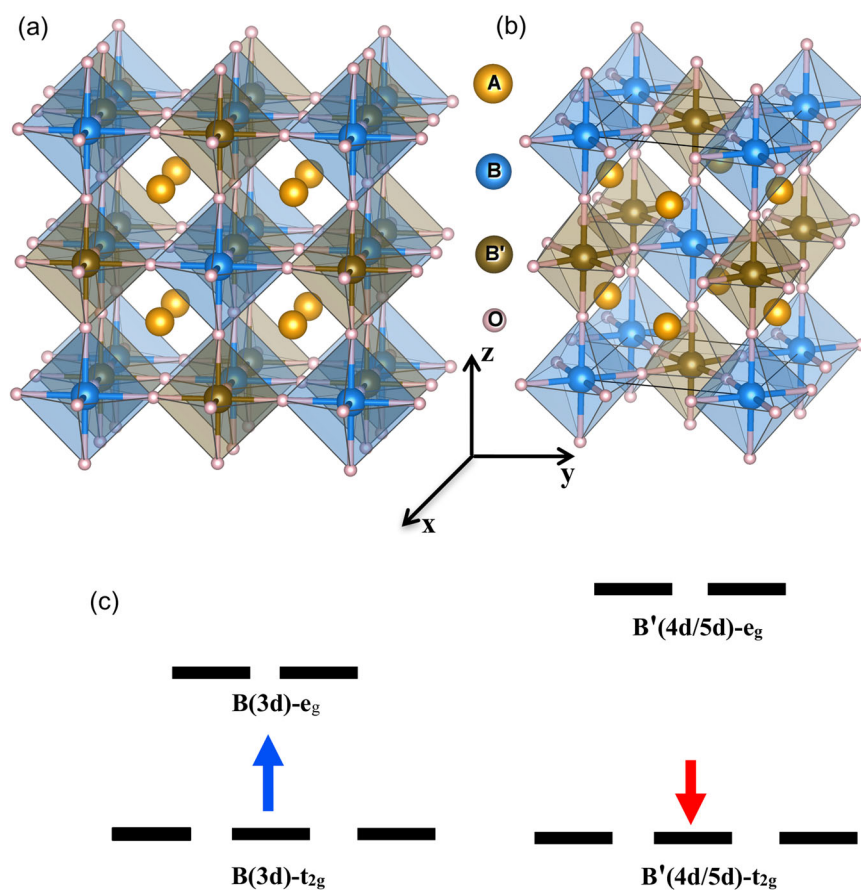
Fig. 1 Crystal structures and schematic energy level diagram. Crystal structure of **a** cubic space group Fm-3m (No. 225) and **b** tetragonal space group I4/m (No. 87) double perovskites. **c** Schematic energy level diagram of the d-levels in the cubic octahedron crystal field at the 3d B and 4d/5d B' sites. The arrows indicate the direction of magnetic moment at the B and B' magnetic sites.

RESULTS AND DISCUSSION

Electronic structures and magnetic ground state

In the present study, we systematically investigated 3d-4d/5d-based cubic and tetragonal stable DP compounds in an attempt to identify and further our understanding of stable magnetic topological quantum materials with large AHC. The primary structural building blocks of the considered compounds are the corner-sharing B(3d)-O_6 and B'(4d/5d)-O_6 octahedra (cf. Fig. 1a, b). As a result of the tetragonal distortion, the octahedra in a tetragonal DP are slightly distorted, whereas they are perfect octahedra in a cubic DP. In the cubic crystal field of regular octahedra, the d-orbitals split into a higher energy level of two-fold (four-fold including spin) degenerate e_g orbitals and a lower energy level of three-fold (sixfold including spin) degenerate t_{2g} orbitals, as schematically shown in Fig. 1c. The electron-electron correlation is expected to decrease from 3d to 4d to 5d transition metal (TM) elements, whereas the bandwidth and spin-orbit coupling strength increases from 3d to 4d to 5d TM elements owing to the enhanced delocalization of electronic wave functions and the higher atomic number (Z), respectively. Consequently, exchange splitting at the 3d-B site is likely to be quite large. However, the crystal field splitting at the 4d/5d-B' site is expected to be very large relative to the exchange splitting owing to the strong delocalization of the electronic wave function. Large crystal field splitting at the 4d/5d-B' site results in the stabilization of the low spin state, and when the 4d/5d-B' orbital is less than or equal to half filled, the empty e_g orbitals would lie far above the Fermi level, with a negligible impact on the electronic structure and transport properties. The main contributing orbitals around the

Fermi energy would be the three 4d/5d-t_{2g} orbitals with strong SOC. In general, the energetically filled 3d orbitals of the B sites, lie below the Fermi energy, which has a finite degree of hybridization with the occupied 4d/5d-t_{2g} orbitals through the O-p orbitals.

From both an experimental and theoretical perspective, it is important to have a topological material with a clean band structure with a topological crossing near the Fermi energy. Depending on the electron occupation of the 3d orbitals of the B site (thereby effectively controlling the exchange splitting), which lie below the Fermi energy, we can effectively control the mixing of the occupied 3d orbitals with the partially occupied 4d/5d-t_{2g} states. In the present study, we considered 3d-4d/5d-based cubic and tetragonal DPs with 0, 1, 2, or 3 electrons in the 4d/5d-t_{2g} state near the Fermi energy, which can provide strong SOC and many electrons in the 3d B sites. Our calculations indicated that whenever B-3d magnetic sites have fully half-filled d-shells or half-filled e_g states, because of the enhanced exchange splitting, the filled 3d orbitals are pushed below the Fermi energy, significantly reducing mixing with the occupied 4d/5d-t_{2g} states. As a result, a clean band structure with predominant 4d/5d-t_{2g} orbitals character is observed around the Fermi energy. For example, in Fig. 2a, b, we present the band structure of Sr_2CoReO_6 and Ba_2NiReO_6 with electron occupancy at the B and B'-sites of Co-d^7, Ni-d^8, and Re-d^1, respectively. Owing to the completely half-filled Ni-e_g states in the compound, we observed a clean band structure with predominantly partially filled Re-t_{2g} states near the Fermi energy compared to the Sr_2CoReO_6 compound.

In the following section, we describe the magnetic ground state, charge state, electron occupancies, and filling of d-orbitals
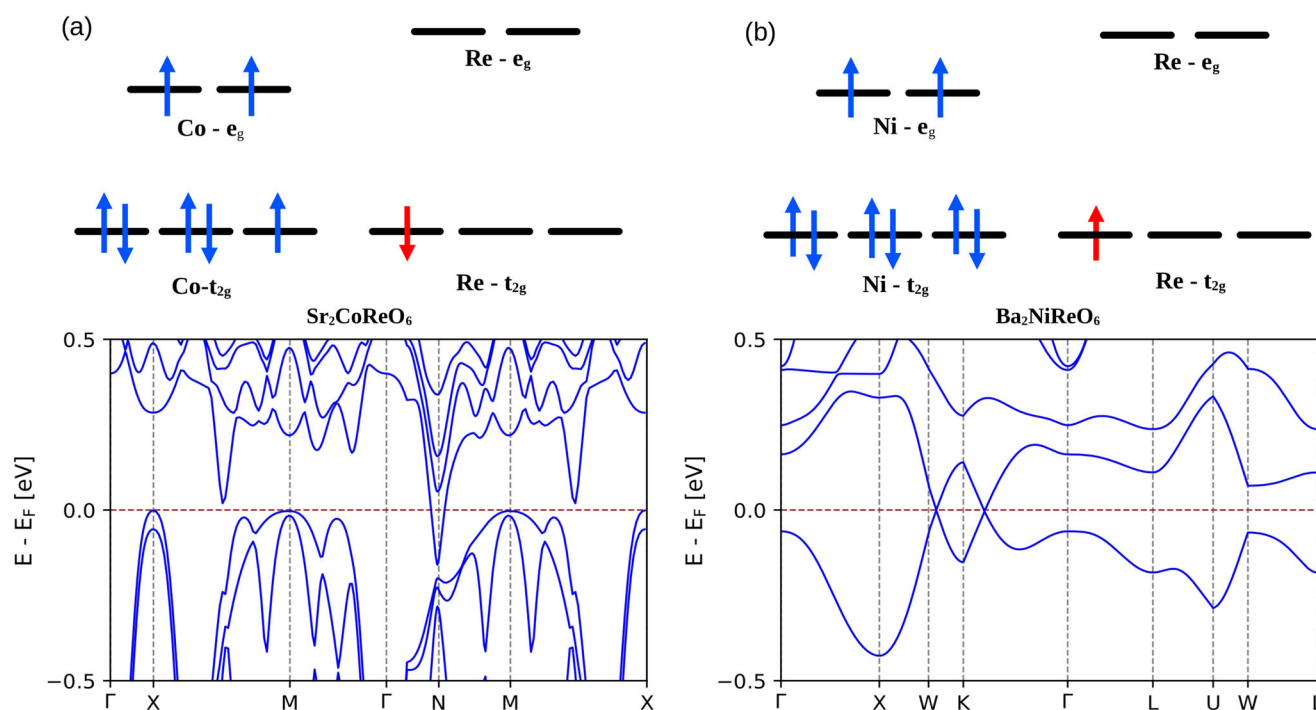
Fig. 2 Effect of 3d orbital filling on the electronic structure. Schematic energy level diagram, orbital filling of the d-levels in the octahedron crystal field at the Co/Ni-3d and Re-5d sites and band structure with SOC for **a** tetragonal double perovskites, Sr_2CoReO_6, and **b** cubic double perovskites, Ba_2NiReO_6.

for the considered DP compounds. In order to understand the magnetic ground state for the DP compounds, we first compared the total energy of their non-magnetic, ferromagnetic, and ferrimagnetic structures. In Supplementary Table 1, we summarize the total energy calculations for the different magnetic structures. The bold entries indicate magnetic ground states for each DP compound. In addition, we calculated magnetic exchange interactions (J) between magnetic elements B-3d and B'-4d/5d to further confirm and understand the magnetic ground state. The calculated exchange coupling constants (J) as a function of the distance between B-3d and B'-4d/5d elements for all the considered DP compounds are summarized in Supplementary Figs. 2, 3. A negative sign in the exchange interactions between B-3d and B'-4d/5d in Supplementary Figs. 2, 3 indicates a ferrimagnetic ground state, and a positive sign indicates a ferromagnetic alignment. From the estimated exchange coupling, we further calculated the magnetic transition temperature T_c using the mean field formula[50] for all the DP compounds. In Supplementary Table 2, we summarize the mean field estimated T_c for all the considered DP compounds. We also compared the mean field estimate of the magnetic transition temperature of the DP compounds with the experimentally reported magnetic transition temperature (cf. Supplementary Table 2) and for most of the DP compounds, the mean field[50] estimated T_c is found to be underestimated compared to that of the reported measured magnetic transition temperature.

Considering the magnetic ground state structure, we did electronic structure calculations for all the considered DP compounds. In order to understand the detailed electronic structure, B-3d and B'-4d/5d orbital occupancies and orbital filling in more detail, the density of states with GGA+U for all the considered DP compounds are shown in Supplementary Figs. 4, 5. In the Fe-based cubic DP, we find a magnetic moment of ~4.0 μ_B, indicating a nominal valency of Fe^{3+} with a high-spin state d^5 occupancy [$t_{2g}(3\uparrow)$, $e_g(2\uparrow)$] consistent with the experimental result reported for the Fe based compounds[51–53]. On the other hand, the calculated density of states (DOS) and magnetic moment

indicated a nominal valency of 2+ at the Mn, Co, and Ni with the following occupancies for d^5 [$t_{2g}(3\uparrow)$, $e_g(2\uparrow)$], d^7 [$t_{2g}(3\uparrow, 2\downarrow)$, $e_g(2\uparrow)$] and d^8 [$t_{2g}(3\uparrow, 3\downarrow)$, $e_g(2\uparrow)$], respectively. The d-level occupancy at the 4d/5d-B' site of Mo, W, and Re varies from 0 to 2 (cf. Table 1). The low-energy state is primarily governed by the 4d/5d-t_{2g} states (cf. orbital-resolved band structure of the cubic DP in the Supplementary Information). So, it is expected to have a negligible contribution from the 4d/5d-t_{2g} orbital near the Fermi energy for the completely unoccupied 4d/5d-t_{2g} state. Therefore, compounds with half-filled 3d orbitals and completely unoccupied 4d/5d-t_{2g} orbitals usually lead to an insulating solution as found in Ba_2MnMoO_6 and Ba_2NiWO_6.

In the tetragonal group of DP compounds, from the calculated DOS and magnetic moment, the sites occupied by Co, Ni and Fe, Cr are found to be in the charge state 2+ and 3+, respectively, with occupancies of d^7 [$t_{2g}(3\uparrow,2\downarrow)$, $e_g(2\uparrow)$], d^8 [$t_{2g}(3\uparrow, 3\downarrow)$, $e_g(2\uparrow)$], d^5 [$t_{2g}(3\uparrow)$, $e_g(2\uparrow)$], and d^3 [$t_{2g}(3\uparrow)$], respectively. In the group of tetragonal DP compounds, Sr_2NiMoO_6 and Sr_2CrOsO_6 are found to be insulating. In the Sr_2CrOsO_6 compound, both Cr and Os are in the d^3 configuration and aligned anti-parallel to each other. Both completely filled Cr-t_{2g} up the spin channel and Os-t_{2g} down-spin channel lie below the Fermi energy and the empty e_g states of Cr and Os lie above the Fermi energy (cf. orbital-resolved band structure of tetragonal DP in the Supplementary Information). This leads to an insulating solution whereas in the Sr_2NiMoO_6 compound Mo is the d^0 state, thus a negligible contribution around the Fermi energy. The half-filled Ni-e_g states lie below the Fermi energy and give rise to an insulating solution. In Supplementary Table 2, we summarize the detailed charge state of each individual element, electron occupancies, and orbital fillings of each B-3d and B'-4d/5d element of the considered DP compounds.

AHC and ANC of considered DP compounds

Based on the knowledge we gained of the electronic structure and magnetic ground state for all the considered DP compounds, we

Table 1. Summary of the results of selected materials considered in this study.

Material	SG	B-3d site	B'-4d/5d site	B (μ_B)	B' (μ_B)	M (μ_B/f.u.)	MS	AHC (S cm^{-1})	AHC$_{max}$(ΔE) (S cm^{-1})	ANC (A m^{-1} K^{-1})	ANC$_{max}$(ΔE) (A m^{-1} K^{-1})
Ba$_2$FeMoO$_6$	225	Fe^{3+} – 3d^5	Mo^{5+} – 4d^1	3.97	−0.40	3.99	FiM	6.94	37 (0.20)	0.04	−0.18 (0.20)
Ba$_2$CoMoO$_6$	225	Co^{2+} – 3d^7	Mo^{6+} – 4d^0	2.70	0.03	2.99	FM	0.00	0.00	0.00	0.00
Ba$_2$MnMoO$_6$	225	Mn^{2+} – 3d^5	Mo^{6+} – 4d^0	4.54	0.11	4.99	FM	0.00	0.00	0.00	0.00
Ba$_2$FeReO$_6$	225	Fe^{3+} – 3d^5	Re^{5+} – 5d^2	3.90	−0.92	3.06	FiM	33.43	329 (0.20)	0.04	−1.20 (0.14)
Ba$_2$MnReO$_6$	225	Mn^{2+} – 3d^5	Re^{6+} – 5d^1	4.52	−0.66	4.03	FiM	278	536 (0.03)	1.52	−2.10 (0.10)
Ba$_2$NiReO$_6$	225	Ni^{2+} – 3d^8	Re^{6+} – 5d^1	1.70	0.71	2.95	FM	−495	−571 (0.01)	0.220	2.51 (0.05)
Ba$_2$NiWO$_6$	225	Ni^{2+} – 3d^8	W^{6+} – 5d^0	1.71	0.06	2.01	FM	0.00	0.00	0.00	0.00
Sr$_2$NiMoO$_6$	87	Ni^{2+} – 3d^8	Mo^{6+} – 4d^0	1.67	0.07	2.00	FM	0.00	0.00	0.00	0.00
Sr$_2$FeMoO$_6$	87	Fe^{3+} – 3d^5	Mo^{5+} – 4d^1	4.06	−0.55	3.99	FiM	73.68	99 (0.17)	0.03	0.94 (0.16)
Sr$_2$CoOsO$_6$	87	Co^{2+} – 3d^7	Os^{6+} – 5d^2	2.68	−1.18	1.16	FiM	300	517 (0.12)	−1.61	3.13 (0.20)
Sr$_2$CoReO$_6$	87	Co^{2+} – 3d^7	Re^{6+} – 5d^1	2.44	−0.44	2.03	FiM	−22	200 (0.19)	−0.52	−1.97 (0.20)
Sr$_2$CrOsO$_6$	87	Cr^{3+} – 3d^3	Os^{5+} – 5d^3	2.74	−1.79	0.18	FiM	0.00	0.00	0.00	0.00
Sr$_2$NiOsO$_6$	87	Ni^{2+} – 3d^8	Os^{6+} – 5d^2	1.68	1.22	3.84	FM	176	206 (−0.08)	−0.66	−2.60 (−0.19)
Sr$_2$NiReO$_6$	87	Ni^{2+} – 3d^8	Re^{6+} – 5d^1	1.67	−0.65	1.03	FiM	447	447	−0.30	2.54 (0.01)

Listed are the space group (SG), charge state, and electron occupancy at the B-3d and B'-4d/5d sites, the magnetic moment at the B-3d and B'-4d/5d sites, theoretical magnetization per formula unit (f.u.), magnetic ground state (MS), AHC, maximum AHC, ANC, and maximum ANC. The maximum values are obtained in an energy window of 200 meV around the Fermi level. ΔE indicates the energy distance in eV of the maximum values with regard to the Fermi level.

subsequently investigated the topological transport characteristics, AHC and ANC. Table 1 summarizes the calculated AHC and ANC for all the compounds at the Fermi energy and Supplementary Fig. 1 shows a graphic representation. It is clearly evident that the value of AHC and ANC around the Fermi energy is more or less of the same order of magnitude for the cubic and tetragonal group of DP compounds, for example, the cubic DP Ba$_2$NiReO$_6$ and tetragonal DP Sr$_2$NiReO$_6$. To correlate the similar trend that was observed for the AHC and ANC in the cubic and tetragonal group of DP compounds, we investigated their magnetic space group in detail using the FINDSYM[54,55] software package. Considering the SOC with magnetization along 001 direction, the magnetic space groups (MSG) of the cubic and tetragonal DP compounds are determined to be I4/mm'm' and I4/m, respectively. Both MSG have a mirror m_z along the z-axis, and lack m_x and m_y, which is why both cubic and tetragonal DPs present a gapless nodal line at $k_z = 0$ but gapped nodal lines at $k_x = 0$ and $k_y = 0$. However, these gapped nodal lines have a different origin, in the case of cubic DPs m_x and m_y are broken because of the coupling between SOC and magnetism, whereas in the case of tetragonal DPs they were never present. Hence, for the cubic DP compounds, the main source of the Berry curvature around the Fermi energy is found to be the gapped topological nodal line in the presence of SOC and is discussed in more detail in the selected material with a large AHC and ANC section.

Selected material with large AHC and ANC

The calculated value of the AHC of the Ba$_2$NiReO$_6$ is almost three times larger than that of the ferromagnetic SrRuO$_3$, which is a prototype of ferromagnetic oxide materials and has been studied extensively[19,41]. In addition, the determination of the energy dependence of the AHC and ANC is also important to account for the energy shifts away from the Fermi energy. Therefore, we additionally show the largest possible value in a range of 200 meV around the Fermi energy in Table 1. This occurs because minor oxygen nonstoichiometry is commonly found in perovskite oxides[56–58] and has the effect of a small degree of doping and, consequently, a shift in the Fermi level. The largest values of AHC and ANC we found are −571 S cm^{-1} and −2.83 A m^{-1} K^{-1} in
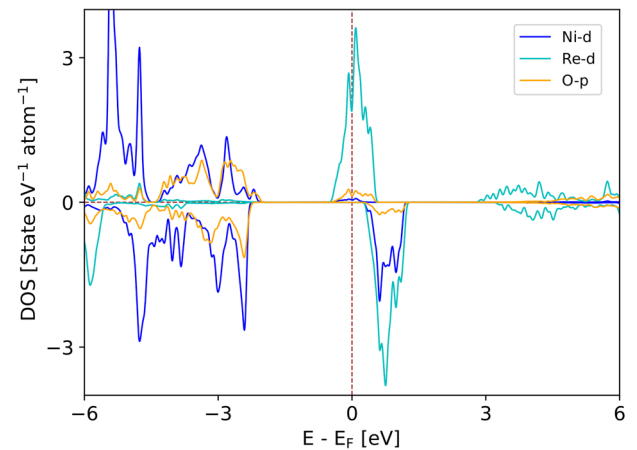

Fig. 3 Site projected DOS. Spin-polarized GGA+U density of states for the DP Ba$_2$NiReO$_6$, projected onto Ni-d (blue), Re-d, (cyan), and O-p (orange) states.

Ba$_2$NiReO$_6$. Results show that changes in the Fermi energy can have a large influence on the anomalous transport coefficients, AHC, and ANC (cf. Supplementary Figs. 14–27). To understand the large anomalous transport coefficients of Ba$_2$NiReO$_6$, we investigated its electronic and magnetic structure and topological features in more detail, and present the results in the following section.

First, using the GGA+U method, we compared the total energies of the different magnetic structures—non-magnetic, ferromagnetic, and ferri-magnetic—to determine the magnetic ground state of DP compounds. The calculations revealed the ferromagnetic ground state to be energetically favorable. The calculated spin-polarized DOS, considering the ferromagnetic ground state with the GGA+U calculation, is shown in Fig. 3. Within the crystal field of a regular octahedron, the d-levels split into t_{2g} and e_g states, and the d-states of Ni and the Re ions are exchanged and the crystal field splits. The exchange splitting at the 3d-Ni site is expected to be high compared to the 5d-Re site, whereas the large crystal field splitting at the 5d-Re site stabilizes
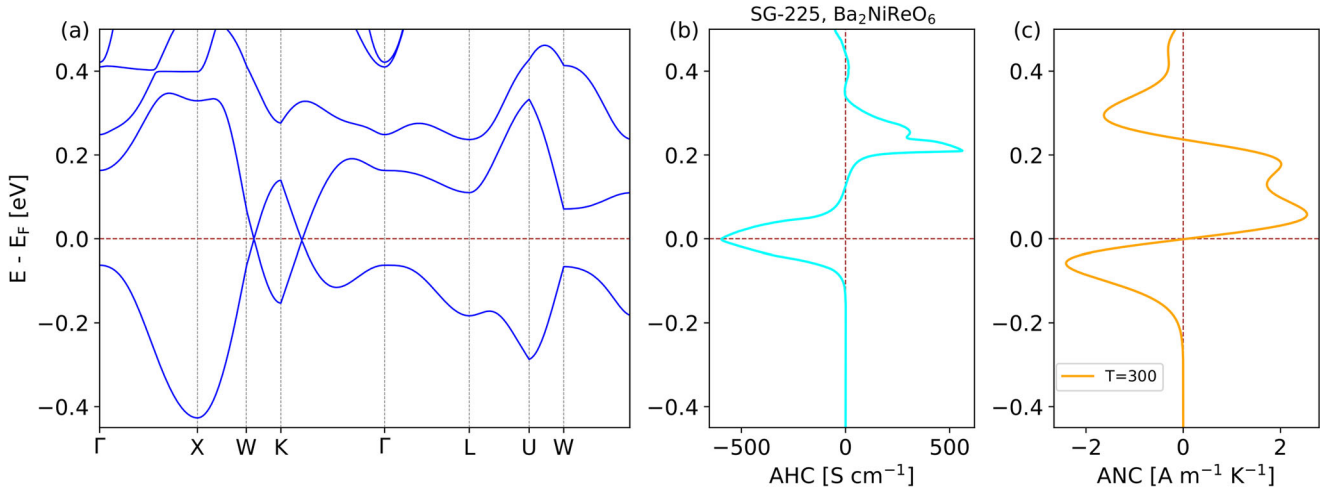
Published in partnership with the Shanghai Institute of Ceramics of the Chinese Academy of Sciences

Fig. 4 Electronic structure, AHC, and ANC. a Band structure in the presence of spin-orbit coupling (SOC) and Hubbard U. **b** anomalous Hall conductivity (AHC), σ, and **c** anomalous Nernst conductivity (ANC), α, for the DP Ba_2NiReO_6.

in the low spin state. The calculations with the GGA+U showed that the localized magnetic moment at the Ni-3d and Re-5d sites is found to be 1.70 and 0.7 μ_B, respectively, which indicates that $Ni^{2+}(3d^8)$ is in the high spin ([$t_{2g}(3\uparrow, 3\downarrow)$ $e_g(2\uparrow)$]) and $Re^{6+}(5d^1)$ in the low spin [$t_{2g}(1\uparrow)$] states. In the DP Ba_2NiReO_6 compound, as Ni is in the high spin d^8 configuration, both the majority and minority spin channels of t_{2g} and the majority spin channel of e_g are completely filled, whereas the minority spin channel of e_g remains completely empty and lies above the Fermi energy (cf. Fig. 3). On the other hand, low spin $Re^{6+}(5d^1)$ has only one electron and, from Fig. 3, it is evident that the states close to the Fermi level (E_F) are mainly contributed by the partially filled Re-[$t_{2g}(1\uparrow)$] states in the up spin channel. The partially filled Re-t_{2g} states cross the Fermi level in the majority spin channel, which causes this spin channel to become conducting. In contrast, a clear gap arises in the minority spin channel, leading to a half-metallic ferromagnetic ground state with full spin polarization. From the orbital-resolved partial DOS (cf. Fig. 3), it is clearly evident that a trivial band gap of 1.2 eV exists in the minority spin channel of Ba_2NiReO_6, whereas that in the majority spin channel contributes significant states to form a peak-like DOS near the Fermi level, which consist mainly of Re-t_{2g} states hybridized with O-2p states.

As the states close to the Fermi energy are dominated by the partially filled Re-t_{2g} states, the effect of the SOC in the electronic structure is expected to be high. The electronic band structure, with the GGA+U+SOC calculations considering the ferromagnetic ground state, is shown in Fig. 4a. With the constructed tight-binding Hamiltonian considering the atomic orbital-like MLWFs of the Ni-d, Re-d, Sr-d, and O-p states, the calculated intrinsic contribution of the AHC and the ANC as a function of the Fermi energy is shown in Fig. 4b, c, respectively. From the computed value of the AHC as a function of Fermi energy, we observed a large peak of the AHC around the Fermi energy (cf. Fig. 4b). We also crosschecked our electronic structure, AHC and ANC calculations for a different choice of U values at the Ni-3d and Re-5d site, but no significant changes were observed in the basic electronic structure and in the peak of AHC and ANC near the Fermi energy (cf. Supplementary Fig. 6). This demonstrates the robustness of our calculation. In the next section, we investigated the peak in the AHC in detail, taking into account the values of $U = 4.0$ and 1.6 eV at Ni-3d and Re-5d sites, respectively.

Detailed topological analysis of selected material

The band structure of the DP Ba_2NiReO_6 undergoes a very distinct change because of the strong SOC of the Re−5d states. Near the

Fermi level, most of the band touching points are gapped. Along the K−Γ direction, the valence and conduction bands of Re-t_{2g} intersect with each other. To understand the topological nature of the band crossing along K−Γ, we examined the electronic structure in more detail. In the absence of magnetism and SOC, the cubic DP Ba_2NiReO_6 preserves m_x, m_y, m_z, C_{4x}, C_{4y}, and C_{4z} symmetries. Without SOC, the internal spin space, and the lattice space are decoupled from each other and spins can be separated into spin-up and spin-down sectors. Thus, in the absence of the SOC, cubic Ba_2NiReO_6 possesses three mirror planes at $k_z = 0$, $k_y = 0$, $k_x = 0$, and symmetry-protected nodal lines can appear in any of the three planes[37,59,60]. Considering the magnetic ground state with GGA+U, we observe the symmetry-protected nodal line in each of the three planes ($k_x = 0$, $k_y = 0$, $k_z = 0$) along the K−Γ direction, as shown with green lines in Fig. 5a–c.

The situation is different when we take into account the SOC, in the presence of which the spin space (coupled up and down-spin channels) and the lattice space are coupled with each other, thus breaking the spin-rotational symmetry. Particularly, when considering the moments aligned along the z-direction, i.e., the magnetization along the 001-direction, the m_x and m_y symmetries are broken, thus breaking the symmetry protection of nodal lines in the $k_x = 0$ and $k_y = 0$ planes, leading to a gapped nodal line along the K−Γ high-symmetry line (cf. Fig. 5c, b). Instead, for the moment aligned along the z-direction, the m_z symmetry is still preserved, which leads to the gapless nodal line in the $k_z = 0$ plane (cf. Fig. 5a). As a result of the gapped nodal lines, a large Berry curvature could be induced in the Brillouin zone (BZ), consequently enhancing the AHC[37,59,60]. Following the above discussion, we expect the nodal lines to be gaped away from the $k_z = 0$ plane, which can lead to the formation of Weyl points. Thus, we searched the Weyl points in the whole Brillouin zone considering the two bands that form the nodal line and found Weyl points near the Fermi energy (35.5 meV above the Fermi energy). In Supplementary Table 3 and Supplementary Fig. 12, we show the coordinates, topological charge, bulk band structure, and surface spectrum showcasing the topologically protected Fermi arc connecting the projection of the Weyl nodes.

We calculated the Berry curvature contribution in the k_x and $k_y = 0$ planes to further investigate the contribution of these gapped nodal lines to the AHC. As expected, due to the presence of the mirror symmetry at the $k_z = 0$ plane with SOC (M ∥ 001), a closed nodal line would be visible and, consequently, the closed nodal line results in an almost zero Berry curvature contribution in the $k_z = 0$ plane. In Fig. 6a, we show the band
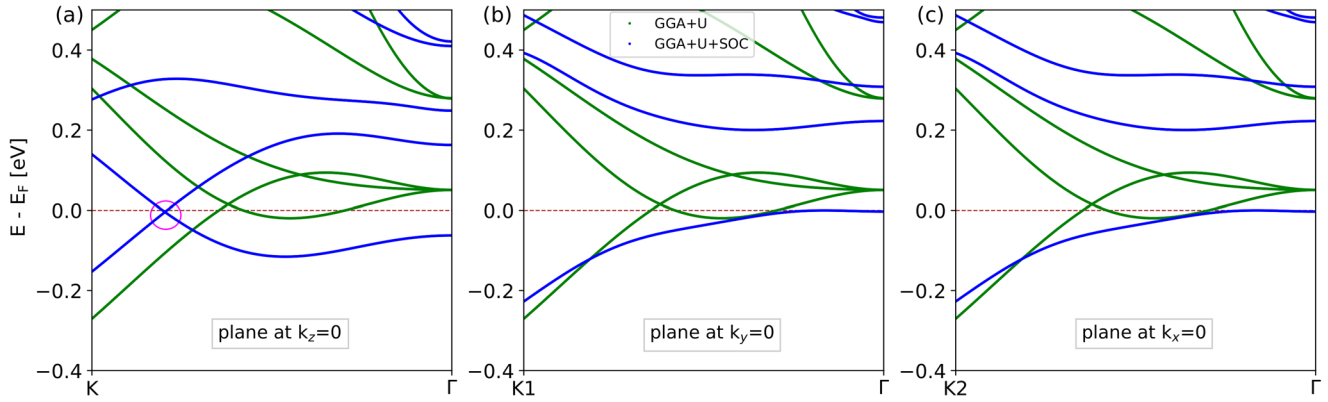
Fig. 5 Symmetry-protected nodal line. Band structure calculated along the K - Γ direction in the planes $k_z = 0$ (**a**), $k_y = 0$ (**b**), and $k_x = 0$ (**c**) for the DP Ba$_2$NiReO$_6$. Green lines: band structure with GGA+U, blue lines: band structure with GGA+U+SOC. In the $k_z = 0$ plane, the crossing indicated by the red circle is intact due to the protected mirror plane while in the $k_x = 0$ or $k_y = 0$ planes, nodal lines gapped out in the presence of SOC (magnetization, M ∥ (001).
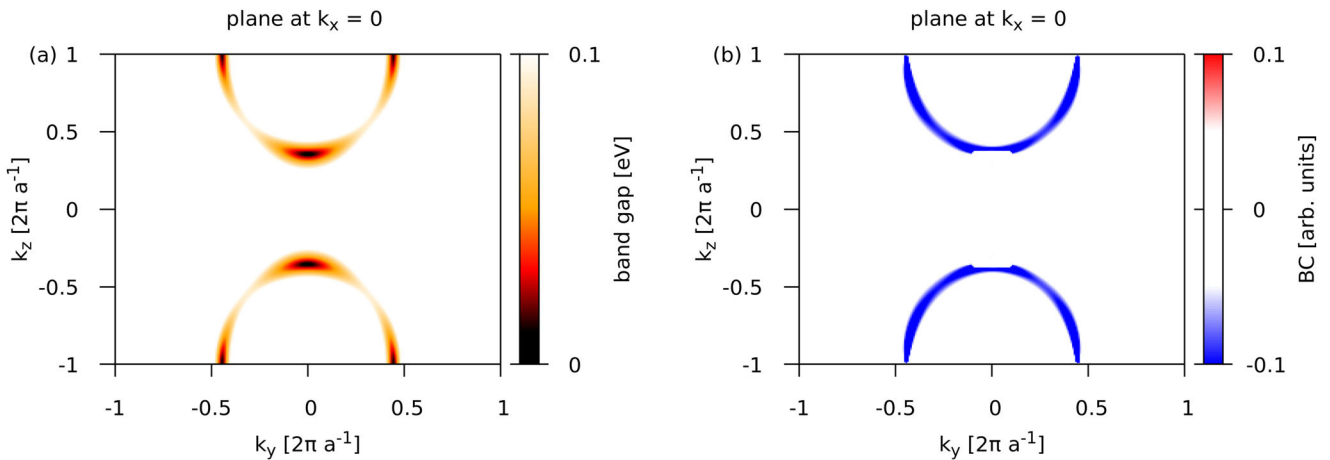

Fig. 6 Gaped nodal line and Berry curvature. a Band gap in the $k_x = 0$ plane with magnetization M∥ (001). The gap structure resembles that of the original nodal line. **b** Berry curvature in the $k_x = 0$ plane with M∥ (001). Strong Berry curvature contribution is visible along the gaped nodal line.

gap in the $k_x = 0$ plane by considering the two bands that form the nodal line for the DP Ba$_2$NiReO$_6$. In the $k_x = 0$ plane, in which the mirror symmetry is broken due to the magnetization along the z-direction (001), the nodal lines are separated by a gap, as shown in Fig. 6a. Consequently, the gapped nodal lines make a large contribution to the Berry curvature in the system, as shown in Fig. 6b. To quantify the contributions that the gapped nodal lines make to the total AHC, we restricted the integration of Eq. (2) to slices around the $k_x = 0$ and $k_y = 0$ planes, as these are the planes in which the gapped lines reside. Considering the thickness of the slices at 20% of the full BZ, we observe that 80 % of the AHC value can be attributed to the gapped nodal line structure of the DP Ba$_2$NiReO$_6$, which suggests that the gapped nodal lines are the primary source of AHC. We further studied the topological crossing and the transport characteristics (AHC and ANC) considering the SOC with magnetization along the 100 and 010 directions. As the cubic DP compounds possess m_x and m_y mirror planes at the k_x and $k_y = 0$ planes, we find a gapless nodal line in the $k_x = 0$ plane for the SOC with magnetization along the 100 while a gapless nodal line is found in the $k_y = 0$ plane for the SOC with magnetization along the 010 (cf. Supplementary Fig. 10). Since the nodal line features remain unchanged for the SOC with magnetization along 001, 100, or 010 directions, the values of the AHC and ANC are expected to be the same, as shown explicitly in Supplementary Fig. 11.

One of the hallmark features of the nodal line compounds are the protected drumhead surface states, consisting of surface states covering the projection of the nodal line on the surface. Therefore, to find the topologically protected surface state of DP Ba$_2$NiReO$_6$, the surface states were calculated using the Wannier-Tools software package[61,62], which employs tight-binding Hamiltonians constructed by maximally localized Wannier functions[63,64]. In the topological nodal line compounds, the topological invariants[65] and, thus, the surface spectrum are protected by crystalline symmetries. Therefore only surfaces that preserve them will show topologically protected surface states[66–68]. In the case of the DP Ba$_2$NiReO$_6$, the mirror symmetry-protected nodal line is observed in the plane $k_z = 0$, thus one could expect a surface state to prevail on the (001) surface. In Fig. 7a we show the projection of the band dispersion onto the (001) surface, following the high-symmetry k-paths shown in Fig. 7b. On the projected (001) surface, topological non-trivial surface states are clearly visible, connecting the two gapless points within $\Gamma_1 - X_1$ and $M_1 - \Gamma_1$ to form a two-dimensional drumhead surface. Moreover, the dispersion of the drumhead surface states is observed to be small compared to other material classes[68,69] and located very close to the Fermi energy, contributing a large surface DOS at the Fermi energy, which is greatly beneficial for experimental realization as well as in spintronics applications[70].
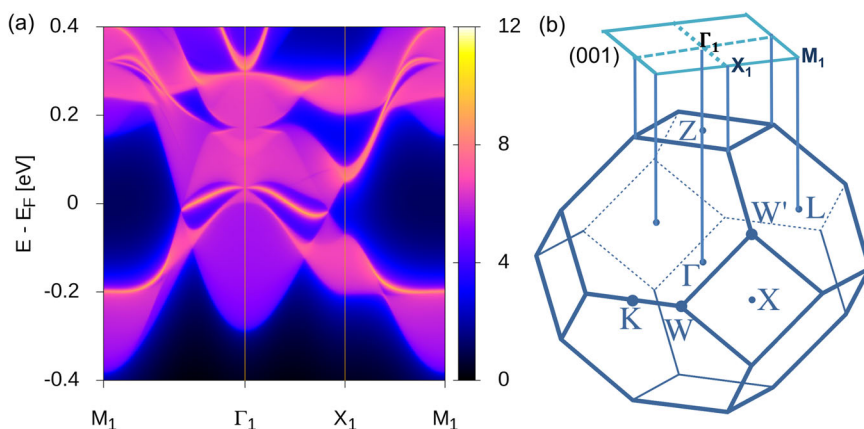
Fig. 7 Topological surface state. a Band dispersion of Ba_2NiReO_6 on the projected (001) surface. **b** BZs of bulk and (001) surfaces with high-symmetry points of the fcc structure.

SUMMARY

In summary, using the first-principles density functional calculations, Wannier interpolation, and symmetry analysis, we have systematically investigated the electronic structure and topological transport characteristics, AHC, and ANC of a list of stable cubic and tetragonal rocksalt ordered DP compounds ($A_2BB'O_6$), with the aim to search and understand stable magnetic topological materials with large AHC and ANC. We presented here a comprehensive study of an intrinsic anomalous transport for the list of representative DP materials considering the 3d TM magnetic ions at the B site and 4d/5d TM magnetic ions at the B' site which provide a high energy scale for magnetism as well as strong spin-orbit coupling and explored the possibility of realizing a clean electronic band structure with a large Berry curvature, hence large AHC and ANC. Our systematic calculations and analysis of the electronic structure for the list of representative DPs materials showed that when DP compounds have a half-filled B site 3d or e_g states and partially filled 4d/5d-t_{2g} states, due to the enhanced exchange splitting at the B sites, mixing with the partially filled 4d/5d-t_{2g} states reduce significantly and leads to the possibility of a clean topological band crossing. This is primarily attributed to strong SOC in the 5d-t_{2g} orbitals near the Fermi energy with large AHC.

From the symmetry analysis, the magnetic space group of the cubic and tetragonal DP compounds considering the SOC with magnetization along z direction, is found to be in the I4/mm'm' and I4/m, respectively, with a mirror symmetry m_z which leads to a symmetry-protected nodal line in the $k_z = 0$ plane. In the presence of magnetism and SOC with magnetization along z direction, m_x and m_y mirror symmetries of the cubic structure are broken, resulting in a gapped topological nodal line in the $k_x = 0$ and $k_y = 0$ planes which are found to be the primary source of the Berry curvature for the cubic DP compounds around the Fermi energy. The presence of mirror symmetries and a clean topological band crossing primarily resulting from the 5d-t_{2g} state with strong SOC, were found to be crucial for large AHC and ANC, which, in combination with the magnetism and SOC, produces a large BC in the band structure.

In certain DP compounds, particularly in Ba_2NiReO_6, we found a symmetry-protected nodal line near the Fermi energy with very large AHC and/or ANC values that are three times larger than the extensively studied prototype metallic ferromagnetic oxide material $SrRuO_3$[19,41]. In the DP Ba_2NiReO_6, slightly dispersing mirror symmetry-protected drumhead surface states and Weyl points are observed around the Fermi energy making it a good candidate for using the topological properties in the spintronics applications. Furthermore, the electronic structure, topological transport characteristics, AHC, and ANC of its optimized structure

are found to remain unchanged, demonstrating the robustness of our calculations. We additionally found that both AHC and ANC are strongly dependent on the position of the Fermi level and, therefore, on the doping level of the investigated material.

This work demonstrates the versatility and usability of cubic and tetragonal DP based on 3d and 4d/5d TM ions to realize a clean topological band crossing near the Fermi energy, primarily resulting from the 4d/5d-t_{2g} state with a large AHC. Our computational study pave the way for high-performance stable magnetic topological materials based on oxide DP.

METHODS

First-principles DFT calculations

For the calculations, we considered stable cubic and tetragonal 3d-4d/5d-based DP compounds whose structural data was taken from the ICSD database[71] with a 3d magnetic element at the B site and 4d/5d magnetic element at the B' site to enable us to investigate topological transport characteristics such as the anomalous Hall and Nernst effects. We considered the experimentally measured lattice constant, atomic position, and space group as inputs for the density functional theory (DFT) calculations. We also checked the calculations with the optimized structures for selected compounds, and found that the electronic structure and transport characteristics, AHC, and ANC almost remain unchanged around Fermi energy (cf. Supplementary Figs. 28, 29 and Supplementary Table 4). The DFT-based plane-wave projected augmented wave (PAW) method, as implemented in the Vienna ab initio simulation package, was employed[72–74]. We used a $12 \times 12 \times 12$ ($12 \times 12 \times 10$) k-points mesh and a plane-wave cutoff of 520 eV, for the self-consistent calculations of cubic (tetragonal) compounds. These selections of the k-mesh and the plane-wave cut-off were found to result in good convergence of the total energy. We used the Perdew-Burke-Ernzerhof (PBE)[75] exchange-correlation functional within the generalized gradient approximation (GGA). The electron-electron correlation effects beyond GGA at the strongly correlated 3d and 4d/5d magnetic sites were taken into account using the supplemented on-site Hubbard U correction via the GGA+U method[76]. Considering that the B site is occupied by a 3d transition metal and the B' site by a 4d/5d transition metal with wider bands compared to the B site, the correlation effect would be expected to be stronger at the B site compared to the B' site. Thus, we chose U values of 4.0 eV and 1.6 eV for the B and B' sites of the considered 3d-4d/5d-based DPs, respectively. The selection of these values was motivated by the U values used for 3d-4d/5d-based DP compounds in previous studies[47–49,77], in which the electronic structure and magnetic ground state were found to be in good agreement with the

experimental results. We initially checked our calculations by varying the U values of a few compounds, but overall, the electronic structure and magnetic ground state remained unaltered. The effect of the SOC is included in the fully relativistic schemes. Magnetic anisotropy calculation (cf. Supplementary Table 5) shows that the z axis (i.e., magnetization along 001) is an easy axis for tetragonal DP compounds, while cubic DP compounds are isotropic in agreement with experimental observation[28]. Thus, for all calculations, magnetization is chosen to be parallel to the (001) direction.

Transport characteristics AHC and ANC calculation

We calculated the contribution of the intrinsic Berry curvature to the anomalous Hall conductivity by employing the Wannier interpolation technique[63]. To compute the Berry curvature, we first constructed maximally localized Wannier functions (MLWFs) Hamiltonian projected from the GGA+U+SOC Bloch wave functions using the Wannier90 tool[64,78,79]. Atomic orbital-like MLWFs of the A-d, B-3d, B'-4d/5d, and O-p states were considered to construct the tight-binding Hamiltonian, which reproduced the spectrum of the system accurately in the energy window of ±2.0 eV around the Fermi energy. The wannierization was repeated with different inner and outer energy windows until it reproduced the spectrum of the system quite accurately in the energy window of ±2.0 eV around the Fermi energy (cf. Supplementary Figs. 44–47).

With the tight-binding model Hamiltonian, we calculated the intrinsic AHC using the linear response Kubo formula approach as follows[80]:

$$\Omega_n^z(\mathbf{k}) = -\hbar^2 \sum_{n \neq m} \frac{2Im\langle u_{n\mathbf{k}}|\hat{v}_x|u_{m\mathbf{k}}\rangle\langle u_{m\mathbf{k}}|\hat{v}_y|u_{n\mathbf{k}}\rangle}{(\epsilon_{m\mathbf{k}} - \epsilon_{n\mathbf{k}})^2}, \quad (1)$$

where $\Omega_n^z(\mathbf{k})$ is the Berry curvature of band n, $\hbar\hat{v}_i = \partial\hat{H}(\mathbf{k})/\partial k_i$ is the i'th velocity operator, $u_{n\mathbf{k}}$ and $\epsilon_{n\mathbf{k}}$ are the eigenstates and eigenvalues of the Hamiltonian $\hat{H}(\mathbf{k})$, respectively.

Subsequently, we calculated the AHC, given by:

$$\sigma_H^A = -\frac{e^2}{\hbar} \sum_n \int_{BZ} \frac{d\mathbf{k}}{(2\pi)^3} f_n \Omega_n^z(\mathbf{k}) \quad (2)$$

and the ANC, α_H^A, as proposed by Xiao et al.[81,82]

$$\alpha_H^A = -\frac{1}{T}\frac{e^2}{\hbar} \sum_n \int_{BZ} \frac{d\mathbf{k}}{(2\pi)^3} \Omega_n^z(\mathbf{k})\left[(E_n - E_F)f_n + k_B T\ln\left(1 + \exp\left(\frac{E_n - E_F}{-k_B T}\right)\right)\right], \quad (3)$$

where T is the actual temperature, f_n is the Fermi distribution, and E_F is the Fermi level. We used a k-point mesh of $300 \times 300 \times 300$ for the calculation of the AHC and ANC using Eqs. (2) and (3), respectively, and $T = 300$ K for the calculation of the ANC.

Magnetic exchange and surface state calculation

In order to compute magnetic exchange interactions (J), we used Green's function approach[83,84], implemented from the combination of the Wannier90[64,78,79] and Tb2j software packages[85]. In this approach, energy variations are utilized due to infinitesimal local spin rotations[83]. Surface states were calculated using tight-binding methods by the combination of the Wannier90[64,78,79] and WannierTools software packages[61,62]. We used the VESTA[86], sumo[87], and PyProcar[88] tools for the lattice structure and projected band structure plots.

DATA AVAILABILITY

All data generated and/or analyzed during this study are included in this article and its Supplementary Information file. The data are available from the corresponding author upon reasonable request.

CODE AVAILABILITY

All code used to calculate the presented results is available from the corresponding author upon reasonable request.

REFERENCES

1. Kane, C. L. & Mele, E. J. Quantum spin hall effect in graphene. *Phys. Rev. Lett.* **95**, 226801 (2005).
2. Bernevig, B. A., Hughes, T. L. & Zhang, S.-C. Quantum spin hall effect and topological phase transition in HgTe quantum wells. *Science* **314**, 1757–1761 (2006).
3. Hasan, M. Z. & Kane, C. L. Colloquium: topological insulators. *Rev. Mod. Phys.* **82**, 3045–3067 (2010).
4. Wieder, B. J. et al. Topological materials discovery from crystal symmetry. *Nat. Rev. Mater.* **7**, 196–216 (2022).
5. Weng, H., Fang, C., Fang, Z., Bernevig, B. A. & Dai, X. Weyl semimetal phase in noncentrosymmetric transition-metal monophosphides. *Phys. Rev. X* **5**, 011029 (2015).
6. Yan, B. & Felser, C. Topological materials: Weyl semimetals. *Annu. Rev. Condens. Matter Phys.* **8**, 337–354 (2017).
7. Armitage, N. P., Mele, E. J. & Vishwanath, A. Weyl and dirac semimetals in three-dimensional solids. *Rev. Mod. Phys.* **90**, 015001 (2018).
8. Xu, S.-Y. et al. Discovery of a weyl fermion semimetal and topological fermi arcs. *Science* **349**, 613–617 (2015).
9. Kitaev, A. Fault-tolerant quantum computation by anyons. *Ann. Phys.* **303**, 2–30 (2003).
10. Pesin, D. & MacDonald, A. H. Spintronics and pseudospintronics in graphene and topological insulators. *Nat. Mater.* **11**, 409–416 (2012).
11. Rajamathi, C. R. et al. Weyl semimetals as hydrogen evolution catalysts. *Adv. Mater.* **29**, 1606202 (2017).
12. Bradlyn, B. et al. Topological quantum chemistry. *Nature* **547**, 298–305 (2017).
13. Cano, J. et al. Topology of disconnected elementary band representations. *Phys. Rev. Lett.* **120**, 266401 (2018).
14. Cano, J. et al. Building blocks of topological quantum chemistry: elementary band representations. *Phys. Rev. B* **97**, 035139 (2018).
15. Vergniory, M. G. et al. A complete catalogue of high-quality topological materials. *Nature* **566**, 480–485 (2019).
16. Vergniory, M. G. et al. All topological bands of all nonmagnetic stoichiometric materials. *Science* **376**, eabg9094 (2022).
17. Xu, Y. et al. High-throughput calculations of magnetic topological materials. *Nature* **586**, 702–707 (2020).
18. Bernevig, B. A., Felser, C. & Beidenkopf, H. Progress and prospects in magnetic topological materials. *Nature* **603**, 41–51 (2022).
19. Fang, Z. et al. The anomalous hall effect and magnetic monopoles in momentum space. *Science* **302**, 92–95 (2003).
20. Wang, R. et al. Ferromagnetic weyl fermions in CrO₂. *Phys. Rev. B* **97**, 195157 (2018).
21. Xia, B. W. et al. Robust twin pairs of weyl fermions in ferromagnetic oxides. *Phys. Rev. Lett.* **122**, 057205 (2019).
22. Samanta, K. et al. Crystal hall and crystal magneto-optical effect in thin films of SrRuO₃. *J. Appl. Phys.* **127**, 213904 (2020).
23. Samanta, K., Ležaić, M., Blügel, S. & Mokrousov, Y. Tailoring the anomalous hall effect of SrRuO₃ thin films by strain: a first principles study. *J. Appl. Phys.* **129**, 093904 (2021).
24. Wang, R. et al. Nodal line fermions in magnetic oxides. *Phys. Rev. B* **97**, 241111 (2018).
25. Zhao, X., Guo, P.-j, Ma, F. & Lu, Z.-Y. Coexistence of topological weyl and nodal-ring states in ferromagnetic and ferrimagnetic double perovskites. *Phys. Rev. B* **103**, 085138 (2021).
26. Song, Y.-J. & Lee, K.-W. Symmetry-protected spinful magnetic weyl nodal loops and multi-weyl nodes in 5dⁿ cubic double perovskites ($n = 1, 2$). *Phys. Rev. B* **102**, 035155 (2020).
27. Wang, R., Jin, Y., Xia, B. & Xu, H. Topological quantum states in magnetic oxides. *J. Phys. Chem. Lett.* **11**, 4036–4042 (2020).
28. Chakraborty, T. et al. Berry curvature induced anomalous hall conductivity in the magnetic topological oxide double perovskite Sr₂FeMoO₆. *Phys. Rev. B* **106**, 155141 (2022).
29. Burkov, A. A. Anomalous hall effect in Weyl metals. *Phys. Rev. Lett.* **113**, 187202 (2014).
30. Groenendijk, D. J. et al. Berry phase engineering at oxide interfaces. *Phys. Rev. Res.* **2**, 023404 (2020).

31. Ye, L. et al. Massive dirac fermions in a ferromagnetic kagome metal. *Nature* **555**, 638–642 (2018).

32. Kim, K. et al. Large anomalous hall current induced by topological nodal lines in a ferromagnetic van der waals semimetal. *Nat. Mater.* **17**, 794–799 (2018).

33. Chang, G. et al. Room-temperature magnetic topological weyl fermion and nodal line semimetal states in half-metallic heusler Co$_2$TiX (X=Si, Ge, or Sn). *Sci. Rep.* **6**, 38839 (2016).

34. Noky, J., Xu, Q., Felser, C. & Sun, Y. Large anomalous hall and nernst effects from nodal line symmetry breaking in Fe$_2$MnX (X = P, As, Sb). *Phys. Rev. B* **99**, 165117 (2019).

35. Noky, J., Zhang, Y., Gooth, J., Felser, C. & Sun, Y. Giant anomalous hall and nernst effect in magnetic cubic heusler compounds. *Npj Comput. Mater.* **6**, 77 (2020).

36. Singh, S. et al. Anisotropic nodal-line-derived large anomalous hall conductivity in ZrMnP and HfMnP. *Adv. Mater.* **33**, 2104126 (2021).

37. Robredo, I. et al. Theoretical study of topological properties of ferromagnetic pyrite CoS$_2$. *J. Phys. D.* **55**, 304004 (2022).

38. Schröter, N. B. M. et al. Weyl fermions, fermi arcs, and minority-spin carriers in ferromagnetic CoS$_2$. *Sci. Adv.* **6**, eabd5000 (2020).

39. Nagaosa, N., Sinova, J., Onoda, S., MacDonald, A. H. & Ong, N. P. Anomalous hall effect. *Rev. Mod. Phys.* **82**, 1539–1592 (2010).

40. Noky, J. & Sun, Y. Linear response in topological materials. *Appl. Sci.* **9**, https://arxiv.org/abs/2005.11834 (2019).

41. Sohn, B. et al. Sign-tunable anomalous hall effect induced by two-dimensional symmetry-protected nodal structures in ferromagnetic perovskite thin films. *Nat. Mater.* **20**, 1643–1649 (2021).

42. Samanta, K. & Saha-Dasgupta, T. Rocksalt versus layered ordering in double perovskites: a case study with La$_2$CuSnO$_6$ and La$_2$CuIrO$_6$. *Phys. Rev. B* **95**, 235102 (2017).

43. Philipp, J. B. et al. Structural and doping effects in the half-metallic double perovskite A$_2$CrWO$_6$ (A=Sr, Ba, and Ca). *Phys. Rev. B* **68**, 144431 (2003).

44. Kobayashi, K.-I. et al. Intergrain tunneling magnetoresistance in polycrystals of the ordered double perovskite Sr$_2$FeReO$_6$. *Phys. Rev. B* **59**, 11159–11162 (1999).

45. Coey, J. M. D. Materials for Spin Electronics, 277–297 (Springer Berlin Heidelberg, Berlin, Heidelberg, 2001).

46. Vasala, S. & Karppinen, M. A$_2$BB′O$_6$ perovskites: a review. *Prog. Solid. State Ch.* **43**, 1–36 (2015).

47. Saha-Dasgupta, T. Double perovskites with 3d and 4d/5d transition metals: compounds with promises. *Mater. Res. Express* **7**, 014003 (2020).

48. Samanta, K. & Saha-Dasgupta, T. Comparative study of electronic structure and magnetic properties of osmate double perovskites: Ca$_2$FeOsO$_6$ versus Ca$_2$Co(Ni)OsO$_6$. *J. Phys. Soc. Jpn.* **87**, 041007 (2018).

49. Morrow, R. et al. Magnetism in Ca$_2$CoOsO$_6$ and Ca$_2$NiOsO$_6$: unraveling the mystery of superexchange interactions between 3d and 5d ions. *Chem. Mater.* **28**, 3666–3675 (2016).

50. Kittel, C. Introduction to solid state physics (8th edn.) John Wiley and Son (2014).

51. Feng, H. L. et al. High-temperature ferrimagnetism driven by lattice distortion in double perovskite Ca$_2$FeOsO$_6$. *J. Am. Chem. Soc.* **136**, 3326–3329 (2014).

52. Colis, S. et al. Structural defects in Sr$_2$FeMoO$_6$ double perovskite: experimental versus theoretical approach. *J. Appl. Phys.* **98**, 033905 (2005).

53. Lofland, S., Scabarozi, T., Moritomo, Y. & Xu, S. Magnetism of the double perovskite Sr$_2$FeMoO$_6$. *J. Magn. Magn. Mater.* **260**, 181–183 (2003).

54. H. T. Stokes, D. M. H. & Campbell, B. J. Isotropy software suite. https://stokes.byu.edu/iso/isotropy.php.

55. Stokes, H. T. & Hatch, D. M. Program for identifying the space group symmetry of a crystal. *J. Appl. Cryst.* **38**, 237–238 (2005).

56. Ang, C., Yu, Z. & Cross, L. Oxygen-vacancy-related low-frequency dielectric relaxation and electrical conduction in Bi:SrTiO$_3$. *Phys. Rev. B* **62**, 228 (2000).

57. De Lima, O., Coaquira, J., De Almeida, R., De Carvalho, L. & Malik, S. Magnetic phase evolution in the LaMn$_{1-x}$Fe$_x$O$_{3+y}$ system. *J. Appl. Phys.* **105**, 013907 (2009).

58. Tong, W., Zhang, B., Tan, S. & Zhang, Y. Probability of double exchange between Mn and Fe in LaMn$_{1-x}$Fe$_x$O$_3$. *Phys. Rev. B* **70**, 014422 (2004).

59. Noky, J., Xu, Q., Felser, C. & Sun, Y. Large anomalous hall and nernst effects from nodal line symmetry breaking in Fe$_2$MnX (X= P, As, Sb). *Phys. Rev. B* **99**, 165117 (2019).

60. Sohn, B., Lee, E., & Park, S. Y. et al. Sign-tunable anomalous hall effect induced by two-dimensional symmetry-protected nodal structures in ferromagnetic perovskite thin films. *Nat. Mater.* **20**, 1643–1649 (2021).

61. Sancho, M. P. L., Sancho, J. M. L. & Rubio, J. Quick iterative scheme for the calculation of transfer matrices: application to Mo(100). *J. Phys. F: Met. Phys.* **14**, 1205–1215 (1984).

62. Wu, Q., Zhang, S., Song, H.-F., Troyer, M. & Soluyanov, A. A. Wanniertools: an open-source software package for novel topological materials. *Comput. Phys. Commun.* **224**, 405–416 (2018).

63. Wang, X., Yates, J. R., Souza, I. & Vanderbilt, D. Ab initio calculation of the anomalous hall conductivity by wannier interpolation. *Phys. Rev. B* **74**, 195118 (2006).

64. Pizzi, G. et al. Wannier90 as a community code: new features and applications. *J. Condens. Matter Phys.* **32**, 165902 (2020).

65. Fang, C., Chen, Y., Kee, H.-Y. & Fu, L. Topological nodal line semimetals with and without spin-orbit coupling. *Phys. Rev. B* **92**, 081201 (2015).

66. Weng, H. et al. Topological node-line semimetal in three-dimensional graphene networks. *Phys. Rev. B* **92**, 045108 (2015).

67. Yu, R., Weng, H., Fang, Z., Dai, X. & Hu, X. Topological node-line semimetal and dirac semimetal state in antiperovskite Cu$_3$PdN. *Phys. Rev. Lett.* **115**, 036807 (2015).

68. Muechler, L. et al. Modular arithmetic with nodal lines: Drumhead surface states in ZrSiTe. *Phys. Rev. X* **10**, 011026 (2020).

69. Bian, G. et al. Drumhead surface states and topological nodal-line fermions in TlTaSe$_2$. *Phys. Rev. B* **93**, 121113 (2016).

70. Zhang, R.-W., Zhang, Z., Liu, C.-C. & Yao, Y. Nodal line spin-gapless semimetals and high-quality candidate materials. *Phys. Rev. Lett.* **124**, 016402 (2020).

71. Inorganic Crystal Structure Database (ICSD). (Fachinformationszentrum Karlsruhe, Karlsruhe, Germany, 2015).

72. Kresse, G. & Furthmüller, J. Efficient iterative schemes for ab initio total-energy calculations using a plane-wave basis set. *Phys. Rev. B* **54**, 11169–11186 (1996).

73. Kresse, G. & Joubert, D. From ultrasoft pseudopotentials to the projector augmented-wave method. *Phys. Rev. B* **59**, 1758–1775 (1999).

74. Blöchl, P. E. Projector augmented-wave method. *Phys. Rev. B* **50**, 17953–17979 (1994).

75. Perdew, J. P., Burke, K. & Ernzerhof, M. Generalized gradient approximation made simple. *Phys. Rev. Lett.* **77**, 3865–3868 (1996).

76. Anisimov, V. I., Aryasetiawan, F. & Lichtenstein, A. I. First-principles calculations of the electronic structure and spectra of strongly correlated systems: the LDA+U method. *J. Condens. Matter Phys.* **9**, 767–808 (1997).

77. Samanta, K., Sanyal, P. & Saha-Dasgupta, T. Half-metallic behavior in doped Sr$_2$CrOsO$_6$ double perovskite with high transition temperature. *Sci. Rep.* **5**, 15010 (2015).

78. Marzari, N., Mostofi, A. A., Yates, J. R., Souza, I. & Vanderbilt, D. Maximally localized wannier functions: theory and applications. *Rev. Mod. Phys.* **84**, 1419–1475 (2012).

79. Souza, I., Marzari, N. & Vanderbilt, D. Maximally localized wannier functions for entangled energy bands. *Phys. Rev. B* **65**, 035109 (2001).

80. Yao, Y. et al. First principles calculation of anomalous hall conductivity in ferromagnetic bcc Fe. *Phys. Rev. Lett.* **92**, 037204 (2004).

81. Xiao, D., Yao, Y., Fang, Z. & Niu, Q. Berry-phase effect in anomalous thermoelectric transport. *Phys. Rev. Lett.* **97**, 026603 (2006).

82. Xiao, D., Chang, M.-C. & Niu, Q. Berry phase effects on electronic properties. *Rev. Mod. Phys.* **82**, 1959–2007 (2010).

83. Korotin, D. M., Mazurenko, V. V., Anisimov, V. I. & Streltsov, S. V. Calculation of exchange constants of the heisenberg model in plane-wave-based methods using the green's function approach. *Phys. Rev. B* **91**, 224405 (2015).

84. Liechtenstein, A., Katsnelson, M., Antropov, V. & Gubanov, V. Local spin density functional approach to the theory of exchange interactions in ferromagnetic metals and alloys. *J. Magn. Magn. Mater.* **67**, 65–74 (1987).

85. He, X., Helbig, N., Verstraete, M. J. & Bousquet, E. Tb2j: A python package for computing magnetic interaction parameters. *Comput. Phys. Commun.* **264**, 107938 (2021).

86. Momma, K. & Izumi, F. *VESTA3* for three-dimensional visualization of crystal, volumetric and morphology data. *J. Appl. Crystallogr.* **44**, 1272–1276 (2011).

87. Ganose, A. M., Jackson, A. J. & Scanlon, D. O. sumo: command-line tools for plotting and analysis of periodic ab initio calculations. *J. Open Source Softw.* **3**, 717 (2018).

88. Herath, U. et al. Pyprocar: a python library for electronic structure pre/post-processing. *Comput. Phys. Commun.* **251**, 107080 (2020).

ACKNOWLEDGEMENTS

AUTHOR CONTRIBUTIONS

K.S. performed all the calculations and analyzed the results with the help of I.R. and J.N. K.S. wrote the manuscript. C.F. conceived the project and M.G.V. supervised the project. All the authors discussed the results and commented on the paper.

COMPETING INTERESTS

The authors declare no competing financial interests.

ADDITIONAL INFORMATION

Supplementary information The online version contains supplementary material available at https://doi.org/10.1038/s41524-023-01106-4.

Correspondence and requests for materials should be addressed to Kartik Samanta, Maia G. Vergniory or Claudia Felser.

Reprints and permission information is available at http://www.nature.com/reprints

Publisher's note Springer Nature remains neutral with regard to jurisdictional claims in published maps and institutional affiliations.